Effects of strong anchoring on the dynamic moduli of heterogeneous nematic polymers

Eric P. Choate · Zhenlu Cui · M. Gregory Forest

Abstract We focus on the linear viscoelastic response of heterogeneous nematic polymers to small amplitude oscillatory shear, paying special attention to the macroscopic influence of strong plate anchoring conditions. The model consists of the Stokes hydrodynamic equations with viscous and nematic stresses, coupled to orientational dynamics and structure driven by the flow gradient, an excluded-volume potential, and a two-constant distortional elasticity potential. We show that the dynamical response simplifies when plate anchoring is either tangential or homeotropic, recovering explicitly solvable Leslie–Ericksen–Frank behavior together with weakly varying order parameters across the plate gap. With these plate conditions, we establish "model consistency" so that all experimental driving conditions (plate-controlled velocity [strain] or shear stress, imposed oscillatory pressure) yield identical dynamic moduli for the same material parameters and anchoring conditions, eliminating the culpability of device influence in scaling behavior. Two physical predictions emerge that imply significant macroscopic elastic and viscous effects controlled by plate anchoring relative to flow geometry: (1)

The storage modulus is enhanced by two to three orders of magnitude for homeotropic relative to parallel anchoring, across all frequencies. (2) The loss modulus exhibits enhancement of a factor of two to three for homeotropic over tangential anchoring, restricted to low frequencies. We further deduce a scaling law for the dynamic moduli versus anisotropy of the distortional elasticity potential.

Keywords Nematic liquid crystal polymers · Linear viscoelasticity · Strong anchoring

E. P. Choate (✉)
Department of Mathematics, Industrial Mathematics Institute,
NanoCenter, University of South Carolina,
Columbia, SC 29208, USA
e-mail: choate@math.sc.edu

Z. Cui
Department of Mathematics and Computer Science,
Fayetteville State University,
Fayetteville, NC 28301, USA

M. G. Forest
Department of Mathematics, Institute for Advanced Materials,
University of North Carolina at Chapel Hill,
Chapel Hill, NC 27599-3250, USA

Introduction

The main goal of this paper is to analytically probe the sensitivity of macroscopic properties of nematic liquid crystal polymers in small amplitude oscillatory shear flow to orientational plate anchoring conditions. Anchoring conditions have been predicted to modify the flow profiles across the plate gap but only at higher plate speeds (Forest et al. 2004; Zhou and Forest 2006, 2007). In this paper, we explore the macroscopic influence and sensitivity to orientational anchoring by assessment of the storage and loss moduli in a small amplitude oscillatory shear experiment.

The side-chain liquid crystal polymer experiments of Rubin et al. (1995) show a decrease in the bulk elasticity at low frequencies due to orientation both in terms of the nematic phase relative to the isotropic phase and also a further reduction for the "aligned" nematic phase relative to other nematic phases. Although we do not address the isotropic case, we predict that the orientation of a nematic phase can play a major role in determining the strength of the frequency-dependent storage moduli. These properties are reminiscent of the observations of Mather et al. (1997) where an imposed shear flow can drive an isotropic–

nematic transition. Mendil et al. (2006) observed experimentally for side-chain liquid crystal polymers that the bulk elasticity of a sample can be greatly increased by changing the plate anchoring conditions. Again, we do not claim to predict their results, but our predictions are similar in the sense of finding "container-based" elastic effects; that is, the elastic effects of the material depend upon the surface interactions and mesoscopic anchoring orientation with its container.

We are also motivated by the main-chain liquid crystal polymer experiments of Colby et al. (2002), which indicate nearly elastic response of strongly heterogeneous nematic polymers. We likewise do not claim to predict their results, as we have no embedded defects that are alluded to in those experiments, but we are able to see a trend toward enhanced elastic moduli both due to heterogeneity of the orientation and velocity fields and due to modifications in plate anchoring conditions.

In the absence of flow, identical strong anchoring conditions at both parallel plates determine a steady-state orientation between the plates that is uniform across the gap, thereby extending the anchoring conditions throughout the interior of the fluid. Using asymptotic perturbation analysis, we solve the boundary value problem for various experimental protocols corresponding to oscillatory shear of nematic polymers with matched anchoring conditions at each plate. We predict significant differences in the measurable macroscopic responses induced by plate anchoring conditions. We can make quantitative predictions when nematic anchoring is either parallel or perpendicular to the plates (equivalently, aligned with the flow or the flow gradient axes). For example, we find that a 1,000-fold increase in the storage modulus arises for normal versus tangential anchoring, and we find the order parameters and associated focusing or defocusing of the orientational distribution are essentially suppressed with these two special wall anchoring conditions.

Burghardt (1991) and de Andrade Lima and Rey (2006) used Leslie–Ericksen–Frank theory under the single elastic constant approximation to study oscillatory shear flows of liquid crystals between two parallel plates. In each case, they considered only fixed homeotropic (normal to the plate surface) anchoring. In addition, de Andrade Lima and Rey (2004a, b) examined tangential anchoring of an oscillatory Poiseuille (pressure-driven) flow in a cylindrical pipe; however, their definitions of the dynamic moduli are slightly different than plane shear flow, making the direct comparison of their results for these two different boundary conditions non-transparent. We do, however, find qualitatively similar results to their studies when these geometrical issues are taken into account. These four studies included spatial distortions in the director angle generated by isotropic distortional elasticity and flow feedback.

To provide a better framework for comparison of these two anchoring conditions and for modeling of a nematic polymer in small amplitude oscillatory shear, we extend their analysis to allow for excluded-volume effects (variations in the order parameters that describe the degrees of orientation with respect to the directors), unequal Frank elasticity constants with an anisotropic Marrucci–Greco potential, and a parametrized strong anchoring condition. A salient consequence of our analysis is that, for precisely two special conditions, homeotropic and tangential anchoring, the flow-orientation tensor model reduces to the Leslie–Ericksen–Frank model; that is, the full system decouples into two smaller systems, one for the order parameters and another for the liquid-crystal-like response of the nematic director and primary flow. Each 2×2 system is explicitly solvable, giving all dynamical response functions and exact frequency scaling laws of the storage and loss moduli. We note that explicit solvability is a huge advantage in which, otherwise, one must solve a boundary value problem for a 4×4 system at each frequency, extract the in-phase and out-of-phase responses, and then fit power laws to the data to infer scaling behavior. Furthermore, for these two special plate anchoring conditions, we are able to establish what one might call "rheological equivalence" between typical experimental protocols and devices. Namely, we formulate the flow-nematic polymer field equations and boundary conditions in such a way that *the same moduli predictions arise for oscillatory flow (or strain), stress, and pressure driving conditions*. To our knowledge, this "textbook issue" is not in the literature, and so we include it for posterity.

Another gap that we wish to bridge in this paper is to extend the mesoscopic tensor analysis for nematic monodomains studied by Larson and Mead (1989) and Choate and Forest (2006) to include heterogeneous tensor responses and the self-consistent hydrodynamic feedback that arises from distortional elasticity. We find important qualitative differences in the storage modulus between the monodomain predictions and our present discussion of heterogeneity with either normal or tangential strong anchoring conditions. We cannot solve the heterogeneous flow-orientation tensor model with tilted anchoring without an extensive numerical study. To get some indication of the disparity between tilted anchoring and the special parallel or perpendicular anchoring, we return to the monodomain problem. Indeed, we find a different frequency scaling law for the loss modulus of a monodomain with tilted anchoring. The present analysis also extends our results on heterogeneity for isotropic (Zhou and Forest 2006) and anisotropic (Cui et al. 2006) elasticity in steady shear flows, from the zero frequency limit to the full spectrum.

Finally, we demonstrate procedures by which we may infer the Leslie tumbling parameter and a measure of the relative strength of the anisotropic distortional elasticity from measurements of the storage and loss moduli.

Model formulation and dimensional analysis

We consider oscillatory flow between parallel plates driven either by drag from moving plates or by pressure gradients. To establish equivalence between these two classes of shear flow with respect to measuring and modeling of dynamic storage and loss moduli, it is necessary to introduce slightly different geometrical labeling for the two flows. The separation of the plates is h for plate-driven shear flow and $2h$ for pressure-driven Poiseuille flow, as depicted in Fig. 1. In each case, we nondimensionalize the gap dimension y by h and choose $y=0$ to correspond to the midpoint of the gap. This choice, in essence, identifies the bottom half of a pressure-driven response with the full gap of a plate-induced response.

To make contact with scaling analysis of Burghardt (1991) and Andrade Lima and Rey (2006), the characteristic stress is chosen to be the so-called Frank stress,

$$\tau_F = \frac{K}{h^2} = \frac{vkTN\mathcal{L}^2 s_0^2}{8h^2}, \qquad (1)$$

where K is the Frank elasticity constant, ν is the polymer number density, k is the Boltzmann constant, T is the temperature, $\mathcal{L}$ is the penetration depth of the elasticity potential, N is a dimensionless strength of the excluded volume potential, and s_0 is an equilibrium order parameter defined below (Wang 2002). From the rotational diffusion rate D_r, we define a characteristic Leslie viscosity

$$\eta_0 = \frac{vkTs_0^2}{D_r}, \qquad (2)$$

and then we define the characteristic timescale as

$$t_0 = \frac{\eta_0}{\tau_F} = \frac{8h^2}{N\mathcal{L}^2 D_r}. \qquad (3)$$

The velocity scale is taken to be $\frac{h}{t_0}$. The dimensionless rate-of-strain and vorticity tensors are denoted by $\mathbf{D} = \frac{1}{2}(\nabla\mathbf{v} + \nabla\mathbf{v}^T)$ and $\mathbf{\Omega} = \frac{1}{2}(\nabla\mathbf{v} - \nabla\mathbf{v}^T)$, respectively.
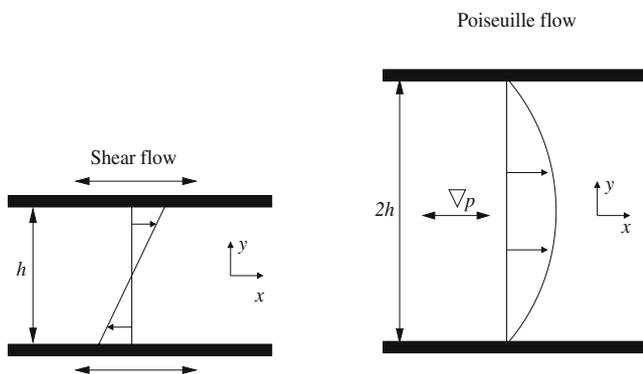

Fig. 1 The flow geometry. For pressure-driven Poiseuille flow, we use a gap width of twice the width of plate-driven shear flow, which proves convenient for comparisons of the two types of experiments

We now identify two nondimensional parameters that arise in the flow-nematic equations and boundary conditions. The *Ericksen number Er* is the ratio of the flow-induced viscous stress to the Frank stress, and the *Deborah number De* is the ratio of the characteristic shear rate to the rotational diffusion rate. These numbers take different forms depending upon the type of flow imposed, which we amplify next.

For plate-driven shear flow, if we impose a stress boundary condition $\tau_{xy}\left(y = \pm\frac{1}{2}\right) = \tau_0\cos\omega t$, then we can use the characteristic viscosity to convert this into the effective shear rate $\dot{\gamma}_{\mathrm{eff}} = \frac{\tau_0}{\eta_0}$, so that

$$Er = \frac{\tau_0}{\tau_F}, \quad De = \frac{\dot{\gamma}_{\mathrm{eff}}}{D_r}. \qquad (4)$$

This definition of Er is consistent with the key papers on Leslie–Ericksen–Frank theory (Burghardt 1991; de Andrade Lima and Rey 2006); however, as there is no molecular relaxation rate in this theory, there is no analogue of De.

For the imposed velocity boundary condition $v_x\left(y = \pm\frac{1}{2}\right) = \pm v_0\cos\omega t$, different definitions must be used (a strain-controlled experiment follows directly by integrating this condition, and identifying the bulk strain with the plate displacement; see below). We can use the gap width h to define a shear rate $\dot{\gamma}_0 = \frac{v_0}{h}$, and then, we can convert this to an effective viscous stress $\tau_{\mathrm{eff}} = \dot{\gamma}_0\eta_0$ to define

$$Er = \frac{\tau_{\mathrm{eff}}}{\tau_F}, \quad De = \frac{\dot{\gamma}_0}{D_r}. \qquad (5)$$

Thus, for plate-induced shear, the nondimensional boundary conditions are

$$\begin{cases} \tau_{xy}\left(y = \pm\frac{1}{2}\right) = Er\cos\omega t, & \text{for imposed stress,} \\ v_x\left(y = \pm\frac{1}{2}\right) = \pm Er\cos\omega t, & \text{for imposed velocity.} \end{cases} \qquad (6)$$

For pressure-driven Poiseuille flow, we use the pressure gradient $\nabla p = \left(\left(\frac{\partial p}{\partial x}\right)_0\cos\omega t, 0, 0\right)$, where $\left(\frac{\partial p}{\partial x}\right)_0$ is constant and negative, and then nondimensionalize so that

$$Er = -\frac{h}{2\tau_F}\left(\frac{\partial p}{\partial x}\right)_0, \quad De = -\frac{h}{2\eta_0 D_r}\left(\frac{\partial p}{\partial x}\right)_0, \qquad (7)$$

and the nondimensional pressure gradient is

$$\nabla p = (2Er\cos\omega t, 0, 0). \qquad (8)$$

For all flows, the above definitions satisfy

$$\frac{Er}{De} = \frac{\eta_0 D_r}{\tau_F} = \frac{t_0}{D_r^{-1}} = \frac{8h^2}{N\mathcal{L}^2} = \alpha. \qquad (9)$$

Whereas the Ericksen number measures the strength of distortional stress relative to the applied stress at the boundary, α represents the relative strengths of the excluded volume potential and the distortional elasticity potential, independent of the driving conditions.

To describe molecular orientation, the primitive variable is **M**, the second moment of the orientational probability density function f, or its traceless part, the orientation tensor $\mathbf{Q} = \mathbf{M} - \frac{\mathbf{I}}{3}$. The dimensionless evolution equation of **M** is given by Wang (2002):

$$
\begin{aligned}
\frac{\partial}{\partial t}\mathbf{M} = {} & \boldsymbol{\Omega} \cdot \mathbf{M} - \mathbf{M} \cdot \boldsymbol{\Omega} + a(\mathbf{D} \cdot \mathbf{M} + \mathbf{M} \cdot \mathbf{D} - 2\mathbf{D} : \mathbf{M}_4) \\
& - 6\alpha[\mathbf{Q} - N(\mathbf{M} \cdot \mathbf{M} - \mathbf{M} : \mathbf{M}_4)] \\
& + \Delta\mathbf{M} \cdot \mathbf{M} + \mathbf{M} \cdot \Delta\mathbf{M} - 2\Delta\mathbf{M} : \mathbf{M}_4 \\
& + \frac{\theta}{2}[(\nabla\nabla\mathbf{M}) \vdots \mathbf{M}_4 + \left((\nabla\nabla\mathbf{M}) \vdots \mathbf{M}_4\right)^T \\
& + \mathbf{M}_4 \vdots \nabla\nabla\mathbf{M} + \left(\mathbf{M}_4 \vdots \nabla\nabla\mathbf{M}\right)^T \\
& + \mathbf{M} \cdot (\nabla\nabla : \mathbf{M}_4) + (\nabla\nabla : \mathbf{M}_4) \cdot \\
& \mathbf{M} - 4\mathbf{M}_6 :: \nabla\nabla\mathbf{M} - 2\mathbf{M}_4 : (\nabla\nabla : \mathbf{M}_4)],
\end{aligned}
$$

(10)

where $\mathbf{M}_4$ and $\mathbf{M}_6$ are the fourth and sixth moments of f, respectively. To close the system for **M** and **v**, we apply the approximations $\mathbf{M}_4 \approx \mathbf{MM}$ and $\mathbf{M}_6 \approx \mathbf{MMM}$. The molecular shape parameter is $a = \frac{R^2-1}{R^2+1}$ where R is the aspect ratio of the spheroidal molecules. Rod-like molecules have $0 < a \leq 1$ and platelets $-1 \leq a < 0$. The parameter $\theta = \frac{L^2}{\mathcal{L}^2}$ measures the anisotropy of molecular elasticity with the interaction length L defined in Wang (2002). Despite the notation, θ can take values in $[-1, \infty)$, being negative for disk-shaped molecules and positive for rods. Additionally, $\theta = 0$ corresponds to the single Frank constant approximation.

If there is no flow and the excluded-volume parameter N is sufficiently high ($N > 3$), then the system is in the nematic phase with the uniaxial equilibrium solution $\mathbf{Q}_0 = s_0\left(\mathbf{n}_0\mathbf{n}_0 - \frac{\mathbf{I}}{3}\right)$, for the equilibrium order parameter $s_0 = \frac{1}{4}\left(1 + 3\sqrt{1 - \frac{8}{3N}}\right)$ and

an arbitrary director $\mathbf{n}_0$. In this paper, we choose $N = 6$ for which $s_0 = 0.809$. We assume strong nematic anchoring at the plates using $\mathbf{Q}_0$ as a boundary condition, parametrizing the degeneracy by a single angle within the flow–flow gradient plane: $\mathbf{n}_0 = (\cos\psi_0, \sin\psi_0, 0)$.

By applying the same uniform plate anchoring conditions on both plates, we find that, in the absences of flow, $\mathbf{Q}(y) \equiv \mathbf{Q}_0$ across the gap, which *extends the influence of the plate anchoring conditions throughout the fluid*. However, by being uniform across the gap, it also allows us to focus on the heterogeneity generated by the deformation.

The dimensionless extra stress tensor $\boldsymbol{\tau}$ from Wang (2002) can be written as the sum of a viscous stress and three types of elastic stress. The viscous stress is

$$
\boldsymbol{\tau}^{\mathrm{Vis}} = \mu_1(\mathbf{D} \cdot \mathbf{M} + \mathbf{M} \cdot \mathbf{D}) + \mu_2\mathbf{D} : \mathbf{M}_4 + \mu_3\mathbf{D} \tag{11}
$$

where $\mu_1 = \frac{3\varsigma_1 D_r}{s_0^2}$, $\mu_2 = \frac{3\varsigma_2 D_r}{s_0^2}$, and $\mu_3 = \frac{2\eta_s}{\eta_0} + \frac{3\varsigma_3 D_r}{s_0^2}$ for the solvent viscosity η_s and the three shape-dependent friction coefficients ζ_i defined in Wang (2002). The nematic elastic stress arises from being out of nematic equilibrium:

$$
\boldsymbol{\tau}^{\mathrm{NE}} = \frac{3a}{s_0^2}\alpha[\mathbf{Q} - N(\mathbf{M} \cdot \mathbf{M} - \mathbf{M} : \mathbf{M}_4)]. \tag{12}
$$

The isotropic distortional elastic stress is

$$
\boldsymbol{\tau}^{\mathrm{IE}} = \frac{1-a}{2s_0^2}\mathbf{M} \cdot \Delta\mathbf{M} - \frac{1+a}{2s_0^2}\Delta\mathbf{M} \cdot \mathbf{M} + \frac{a}{s_0^2}\Delta\mathbf{M} : \mathbf{M}_4 \\
- \frac{1}{4s_0^2}\left(M_{kl,i}M_{kl,j} - \mathbf{M} : \nabla\nabla\mathbf{M}\right),
$$

(13)

and the anisotropic distortional elastic stress is

$$
\boldsymbol{\tau}^{\mathrm{AE}} = \theta\left[\frac{a}{2s_0^2}(2\mathbf{M}_6 :: \nabla\nabla\mathbf{M} + \mathbf{M}_4 : (\nabla\nabla : \mathbf{M}_4)) - \frac{1+a}{4s_0^2}\left(\nabla\nabla\mathbf{M} \vdots \mathbf{M}_4 + \left(\mathbf{M}_4 \vdots \nabla\nabla\mathbf{M}\right)^T + (\nabla\nabla : \mathbf{M}_4) \cdot \mathbf{M}\right) \right. \tag{14}
$$
$$
\left. + \frac{1-a}{4s_0^2}\left((\nabla\nabla\mathbf{M} \vdots \mathbf{M}_4)^T + \mathbf{M}_4 \vdots \nabla\nabla\mathbf{M} + \mathbf{M} \cdot (\nabla\nabla : \mathbf{M}_4)\right)\right].
$$

The dimensionless linear momentum balance is

$$
Re\frac{\partial\mathbf{v}}{\partial t} = \nabla \cdot (-p\mathbf{I} + \tau), \tag{15}
$$

where $Re = \frac{\rho h^2}{\tau_F t_0^2}$ defines a Reynolds number. For liquid crystal polymers, t_0 can be 10^3s or larger, and so with $\rho \approx 10^3$ kg/m³, $h \approx 10^{-4}$m, and $\tau_F \approx 0.1$ Pa, we estimate $Re \approx 10^{-10}$ so that we can safely ignore the fluid inertia term. In our analysis below, the equations are still tractable when

inertia is included, but our solutions confirm the effect is negligible, and so we omit the details.

We analyze the orientation tensor with the spectral representation (Forest et al. 2000; Cui et al. 2006)

$$
\mathbf{Q} = s\left(\mathbf{nn} - \frac{\mathbf{I}}{3}\right) + \beta\left(\mathbf{n}^\perp\mathbf{n}^\perp - \frac{\mathbf{I}}{3}\right), \tag{16}
$$

where (s, β) are two order parameters measuring the birefringence relative to the optical axes (also called directors) $\mathbf{n}$, $\mathbf{n}^\perp$, and $\mathbf{n} \times \mathbf{n}^\perp$; where $\mathbf{n}$ and $\mathbf{n}^\perp$ are assumed

to be confined to the flow (x)-flow gradient (y) plane and parameterized by the director angle ψ as

$$\mathbf{n} = (\cos\psi, \sin\psi, 0), \mathbf{n}^\perp = (-\sin\psi, \cos\psi, 0). \quad (17)$$

Asymptotic analysis

Given the chosen boundary conditions 6 for plate-driven flow and 8 for pressure-driven flow, the appropriate asymptotic limit to examine the linear response is the small Ericksen number limit. Therefore, we propose the solution ansatz for the orientation tensor and flow:

$$
\begin{aligned}
s &= s_0 + \sum_{k=1}^\infty Er^k s^{(k)}(y,t), \\
\beta &= 0 + \sum_{k=1}^\infty Er^k \beta^{(k)}(y,t), \\
\psi &= \psi_0 + \sum_{k=1}^\infty Er^k \psi^{(k)}(y,t), \\
v_x &= 0 + \sum_{k=1}^\infty Er^k v_x^{(k)}(y,t).
\end{aligned}
\quad (18)
$$

Equivalently, we can expand $\mathbf{Q}$ in powers of Er as $\mathbf{Q} = \mathbf{Q}_0 + \sum_{k=1}^\infty Er^k \mathbf{Q}^{(k)}(y,t)$ for which

$$
\mathbf{Q}^{(1)} = s_0 \psi^{(1)}\left(\mathbf{n}_0 \mathbf{n}_0^\perp + \mathbf{n}_0^\perp \mathbf{n}_0\right) + s^{(1)}\left(\mathbf{n}_0\mathbf{n}_0 - \frac{\mathbf{I}}{3}\right)
$$

$$
+ \beta^{(1)}\left(\mathbf{n}_0^\perp \mathbf{n}_0^\perp - \frac{\mathbf{I}}{3}\right). \quad (19)
$$

Additionally, we represent the stress by $\tau = \sum_{k=1}^\infty Er^k \tau^{(k)}$. At $O(Er)$, the systems 10 and 15 transform to

$$
\begin{aligned}
\frac{\partial s^{(1)}}{\partial t} &= 2\alpha\Big((6 - N(s_0+2))s^{(1)} - 2Ns_0(1-s_0)\beta^{(1)}\Big) + \left(\frac{2}{N} + \theta\left(\frac{2(1+s_0)}{3N} - \frac{5+18s_0}{9N}\cos 2\psi_0\right)\right)\frac{\partial^2 s^{(1)}}{\partial y^2} \\
&\quad - \frac{2(1-s_0)}{3}\left(2 + \theta\left(\frac{s_0(s_0+5)}{6} - \frac{8 + 25s_0 + 45s_0^2}{18}\cos 2\psi_0\right)\right)\frac{\partial^2\beta^{(1)}}{\partial y^2} \\
&\quad + \sin 2\psi_0\left(a\frac{1 + 2s_0 - 3s_0^2}{3}\frac{\partial v_x^{(1)}}{\partial y} + \theta\frac{s_0(1+s_0)}{N}\frac{\partial^2\psi^{(1)}}{\partial y^2}\right),
\end{aligned}
\quad (20)
$$

$$
\begin{aligned}
\frac{\partial\beta^{(1)}}{\partial t} &= -6\alpha Ns_0\beta^{(1)} - \sin 2\psi_0\left(a\frac{1-s_0}{3}\frac{\partial v_x^{(1)}}{\partial y} + \frac{\theta s_0}{N}\frac{\partial^2\psi^{(1)}}{\partial y^2}\right) + \frac{4\theta}{9N}\cos 2\psi_0 \frac{\partial^2 s^{(1)}}{\partial y^2} \\
&\quad + \frac{1-s_0}{27}\left(18 + \frac{\theta}{2}\left(4 + s_0 + (10 - 7s_0)\cos 2\psi_0\right)\right)\frac{\partial^2\beta^{(1)}}{\partial^2 y},
\end{aligned}
\quad (21)
$$

$$
\frac{\partial\psi^{(1)}}{\partial t} = -\frac{1}{2}(1 - \lambda_L\cos 2\psi_0)\frac{\partial v_x^{(1)}}{\partial y} + \frac{2+s_0}{3}\left[1 + \frac{\theta s_0}{2}\left(\frac{\lambda_L}{a} - \cos 2\psi_0\right)\right]\frac{\partial^2\psi^{(1)}}{\partial y^2} + \frac{\theta\lambda_L}{36a}\sin 2\psi_0\left((1 + 5s_0)\frac{\partial^2 s^{(1)}}{\partial y^2} + (1 - 4s_0)\frac{\partial^2\beta^{(1)}}{\partial y^2}\right),
\quad (22)
$$

$$
0 = \begin{cases} \dfrac{\partial \tau_{xy}^{(1)}}{\partial y}, & \text{for plate-driven flow,} \\[2mm] 2\cos\omega t + \dfrac{\partial \tau_{xy}^{(1)}}{\partial y}, & \text{for pressure-driven flow,} \end{cases}
\tag{23}
$$

$$
\begin{aligned}
\tau_{xy}^{(1)} = &\left(\frac{\mu_1(s_0+2)}{6} + \frac{\mu_2 s_0^2}{4}\sin^2 2\psi_0 + \frac{\mu_3}{2} \right) \frac{\partial v_x^{(1)}}{\partial y} + \frac{1}{2}\Big[1 - \lambda_L \cos 2\psi_0 \\
&+ \theta\left(\frac{(2+s_0)(1+a)}{6} - \frac{3s_0 + (2+s_0)\lambda_L}{6}\cos 2\psi_0 - \frac{a(2N-3)}{6N}\sin^2 2\psi_0 \right) \Big] \frac{\partial^2 \psi^{(1)}}{\partial y^2} \\
&+ \sin 2\psi_0 \Big[\frac{a\alpha}{2s_0^2}\Big((-6 + N(2+s_0))s^{(1)} + (3 - N(1+2s_0))\beta^{(1)} \Big) \\
&+ \left(-\frac{a}{2Ns_0^2} + \theta\left(\frac{1+5s_0}{72s_0} - a\left(\frac{1+s_0}{6Ns_0^2} + \frac{Ns_0^2 - 18}{48Ns_0^2}\cos 2\psi_0 \right) \right) \right) \frac{\partial^2 s^{(1)}}{\partial y^2} \\
&+ \left(\frac{a(1-s_0^2)}{6s_0^2} - \theta\left(\frac{1-4s_0}{72s_0^2} + a\left(\frac{s_0^3 - 3s_0^2 + 4}{72s_0^2} - \frac{3 - 5s_0^2 + s_0}{24s_0}\cos 2\psi_0 \right) \right) \right) \frac{\partial^2 \beta^{(1)}}{\partial y^2} \Big],
\end{aligned}
\tag{24}
$$

where

$$
\lambda_L = \frac{a(2+s_0)}{3s_0}
\tag{25}
$$

is the Leslie tumbling parameter (Forest and Wang 2003).

Normal and tangential anchoring

At this point, we restrict to two special anchoring conditions, which identify both a dramatic simplification of the model equations 20–24 and a protocol that highlights the most transparent relationship between experimental data and linear viscoelastic moduli. If the anchoring is either parallel to the flow direction (tangential anchoring, $\psi_0 = 0$) or perpendicular to the plates (normal or homeotropic anchoring, $\psi_0 = \frac{\pi}{2}$), then, as observed in Larson and Mead (1989), the nematic elastic stress of a monodomain, which comes only from being out of equilibrium, is zero at leading order. In addition, Choate and Forest (2006) observed that a monodomain under small amplitude oscillatory shear flow will asymptotically drift to oscillations around one of these two orientations—a certain kind of nonequilibrium minimization phenomenon.

These special anchoring conditions provide the significant modeling advantage that the system of four equations 20–24 decouples into two systems of two equations, one for the order parameters and another for the angle and velocity. The order parameter system is

$$
\begin{aligned}
\frac{\partial s^{(1)}}{\partial t} = &\, 2\alpha\Big((6 - N(s_0+2))s^{(1)} - 4Ns_0(1-s_0)\beta^{(1)} \Big) \\
&+ \left(\frac{2}{N} + \theta\left(\frac{2(1+s_0)}{3N} \mp \frac{5+18s_0}{9N} \right) \right) \frac{\partial^2 s^{(1)}}{\partial y^2} - \frac{2(1-s_0)}{3}\left(2 + \theta\left(\frac{s_0(s_0+5)}{6} \mp \frac{8+25s_0+45s_0^2}{18} \right) \right) \frac{\partial^2 \beta^{(1)}}{\partial y^2}, \\
\frac{\partial \beta^{(1)}}{\partial t} = &\, -6\alpha N s_0 \beta^{(1)} \pm \frac{4\theta}{9N}\frac{\partial^2 s^{(1)}}{\partial y^2} + \frac{1-s_0}{27}\left(18 + \frac{\theta}{2}(4 + s_0 \pm (7s_0)) \right) \frac{\partial^2 \beta^{(1)}}{\partial y^2}.
\end{aligned}
\tag{26}
$$

As $s^{(1)}$ and $\beta^{(1)}$ are zero at the boundary of this linear system, we find that $s^{(1)}(y, t) \equiv \beta^{(1)}(y, t) \equiv 0$.

Therefore, for these two anchoring conditions, at leading order, the only elastic stresses are distortional, and the leading order dynamics are dominated by the director angle and velocity. The leading order asymptotic description of the director angle and fluid velocity reduces to the same basic form as those derived for normal anchoring with

liquid crystal theory (Burghardt 1991; de Andrade Lima and Rey 2006):

$$\frac{\partial \psi^{(1)}}{\partial t} = A\Theta(\theta) \frac{\partial^2 \psi^{(1)}}{\partial y^2} + B \frac{\partial v_x^{(1)}}{\partial y}, \qquad (27)$$

$$0 = \begin{cases} \frac{\partial \tau_{xy}^{(1)}}{\partial y}, & \text{for plate-driven flow,} \\ 2\cos\omega t + \frac{\partial \tau_{xy}^{(1)}}{\partial y}, & \text{for pressure-driven flow,} \end{cases} \qquad (28)$$

$$\tau_{xy}^{(1)} = -B\Theta(\theta) \frac{\partial^2 \psi^{(1)}}{\partial y^2} + C \frac{\partial v_x^{(1)}}{\partial y}, \qquad (29)$$

where $A = \frac{s_0+2}{3}$, $C = \frac{\mu_1(s_0+2)}{6} + \frac{\mu_3}{2}$,

$$B = \begin{cases} -\frac{1-\lambda_L}{2}, & \text{if } \psi_0 = 0, \\ -\frac{1+\lambda_L}{2}, & \text{if } \psi_0 = \frac{\pi}{2}, \end{cases} \qquad (30)$$

and where the anisotropy of the molecular elasticity is encoded by

$$\Theta(\theta) = \begin{cases} 1 + \theta \frac{1-s_0}{3}, & \text{if } \psi_0 = 0, \\ 1 + \theta \frac{1+2s_0}{3}, & \text{if } \psi_0 = \frac{\psi}{2}. \end{cases} \qquad (31)$$

As $\theta \geq -1$, it follows that $(AC+B^2)\Theta(\theta) > 0$, and as shown in Cui et al. (2006), all steady solutions of the systems 27–29 are stable for both steady plate-driven and pressure-driven shear flows.

We now observe one additional advantage of the normal and tangential anchoring conditions: The anisotropic distortional elasticity may now be scaled out of the problem by rescaling the characteristic stress as $\tau_F \to \Theta\tau_F$ and time as $t_0 \to \frac{t_0}{\Theta}$. Notice that from Eq. 2, η_0 is unaffected by this rescaling, and from Eqs. 4, 5, and 7, it also rescales the Ericksen number as $Er \to \frac{Er}{\Theta}$.

Furthermore, from Eqs. 1 and 3, this renormalization is equivalent to rescaling $\mathcal{L}^2 \to \Theta\mathcal{L}^2$. *Therefore, at these special anchoring conditions, the effects due to anisotropic distortional elasticity can be absorbed into the isotropic distortional elasticity by a simple scaling law.* This simplification does not hold for tilted anchoring. As $\Theta > 1$ for rods but $0 < \Theta < 1$ for disks, the anisotropic distortional elasticity effectively increases the strength of the isotropic distortional elasticity for rods (as measured by $\mathcal{L}^2$) but decreases it for disks. In both cases, the effect of normal anchoring is stronger than tangential. For the remainder of the paper, we analyze systems 27–29 in the isotropic elastic limit $\theta = 0$ so that $\Theta(\theta) = 1$; results for $\theta \neq 0$ follow from the scaling.

We comment that the above analysis establishes an efficient and transparent protocol for the determination of linear viscoelastic moduli of nematic polymers by controlling plate anchoring; furthermore, as we show below, this

protocol applies to any typical device that imposes strain, velocity, or stress. The realization that the dynamic moduli are anchoring dependent, and indeed strongly so, has not been recognized in the literature to our knowledge *except for the recent papers by Noirez and collaborators* (Pujolle-Robic and Noirez 2001; Mendil et al. 2005, 2006). We emphasize that the inverse characterization of Doi–Marrucci–Greco model parameters does *not* change with anchoring conditions, only the nonequilibrium response of the nematic polymer liquid! Thus, with these special anchoring conditions, the model parameters can be fit independently. Then a comparison of the inverse parameter fits can be made for tangential and homeotropic anchoring, providing a high-level benchmark on the accuracy of the mesoscopic flow-nematic model employed here. If this benchmark is satisfactory, then the full models 20–24 can be studied numerically to ascertain the linear response for arbitrary tilted anchoring conditions, which can be used to estimate the two parameters α and θ that do not enter into the simplified problem with tangential or homeotropic anchoring. A model simulation study of this nature is underway.

Dynamic moduli for plate-driven shear flow

We now establish the stress–strain relationship needed to define the storage and loss moduli for plate-driven shear flow. As systems 27–29 are linear and the plate driving conditions are sinusoidal in time, the standard analysis for determination of the linear viscoelastic moduli is to suppress transients and seek a frequency-locked solution of the form

$$\begin{aligned} \psi^{(1)}(y,t) &= \psi_1(y)\cos\omega t + \psi_2(y)\sin\omega t, \\ v_x^{(1)}(y,t) &= v_1(y)\cos\omega t + v_2(y)\sin\omega t. \end{aligned} \qquad (32)$$

After substituting Eq. 32 into Eqs. 27–29, we obtain the following general solution for the resulting system of ordinary differential equations

$$\begin{aligned} \psi_1(y) &= C_1 \cosh ry \cos ry + C_2 \sinh ry \sin ry - \frac{B}{C\omega}\tau_2, \\ \psi_2(y) &= C_2 \cosh ry \cos ry - C_1 \sinh ry \sin ry + \frac{B}{C\omega}\tau_1, \end{aligned} \qquad (33)$$

$$\begin{aligned} v_1(y) &= -\frac{Br}{C}[(C_1 - C_2)\cosh ry \sin ry \\ &\quad - (C_1 + C_2)\sinh ry \cos ry] + \frac{\tau_1}{C}y, \\ v_2(y) &= -\frac{Br}{C}[(C_1 + C_2)\cosh ry \sin ry \\ &\quad + (C_1 - C_2)\sinh ry \cos ry] + \frac{\tau_2}{C}y, \end{aligned} \qquad (34)$$

where $r = \sqrt{\frac{C\omega}{2(AC+B^2)}}$. Although we have not yet applied boundary conditions to determine the constant coefficients C_1, C_2, τ_1, and τ_2 in Eqs. 33 and 34, we recognize from

Eqs. 28 and 29 that the frequency-locked shear stress is independent of y and takes the form

$$\tau_{xy}^{(1)} = \tau_1 \cos \omega t + \tau_2 \sin \omega t. \tag{35}$$

This conclusion, by itself, is a nontrivial feature of the model in the weak flow asymptotic limit.

For both imposed shear stress and imposed velocity, the director boundary conditions are

$$\psi_1 \left(\pm \frac{1}{2} \right) = 0, \quad \psi_2 \left(\pm \frac{1}{2} \right) = 0. \tag{36}$$

Applying these to Eq. 33 allows us to express C_1 and C_2 as functions of τ_1 and τ_2:

$$C_1 = \tau_1 \frac{2B}{C\omega} \frac{\sin \frac{r}{2} \sinh \frac{r}{2}}{\cosh r + \cos r} + \tau_2 \frac{2B}{C\omega} \frac{\cos \frac{r}{2} \cosh \frac{r}{2}}{\cosh r + \cos r},$$

$$C_2 = -\tau_1 \frac{2B}{C\omega} \frac{\cos \frac{r}{2} \cosh \frac{r}{2}}{\cosh r + \cos r} + \tau_2 \frac{2B}{C\omega} \frac{\sin \frac{r}{2} \sinh \frac{r}{2}}{\cosh r + \cos r}. \tag{37}$$

Plugging these formulas into Eq. 34, we establish a direct relationship between the components of the shear stress and the velocity at the upper plate, which we denote by $V = V_1 \cos \omega t + V_2 \sin \omega t$ where $V_i = v_i\left(\frac{1}{2}\right)$:

$$V_1 = E_2 \tau_1 + E_1 \tau_2 \qquad V_2 = -E_1 \tau_1 + E_2 \tau_2,$$

$$E_1 = \frac{B^2 r}{C^2 \omega} \frac{\sinh r - \sin r}{\cosh r + \cos r}, \quad E_2 = \frac{1}{2C} - \frac{B^2 r}{C^2 \omega} \frac{\sinh r + \sin r}{\cosh r + \cos r}. \tag{38}$$

Therefore, the shear stress 35 and the macroscopic strain $\gamma = \frac{2}{\omega}(V_1 \sin \omega t - V_2 \cos \omega t)$ provide the stress–strain relationship that we need to identify the storage and loss moduli as, respectively,

$$G'(\omega) = \frac{\omega}{2} \frac{\tau_2 V_1 - \tau_1 V_2}{V_1^2 + V_2^2} = \frac{\omega}{2} \frac{E_1}{E_1^2 + E_2^2} = \frac{2B^2 C^2 \omega^2 r (\sinh r - \sin r)}{(8B^4 r^2 + C^2 \omega^2)(\cosh r + \cos r) - 16B^4 r^2 \cos r - 4B^2 Cr\omega(\sin r + \sinh r)}, \tag{39}$$

$$G''(\omega) = \frac{\omega}{2} \frac{\tau_1 V_1 + \tau_2 V_2}{V_1^2 + V_2^2} = \frac{\omega}{2} \frac{E_2}{E_1^2 + E_2^2} = \frac{C^2 \omega^2 (C\omega(\cosh r + \cos r) - 2B^2 r(\sinh r + \sin r))}{(8B^4 r^2 + C^2 \omega^2)(\cosh r + \cos r) - 16B^4 r^2 \cos r - 4B^2 Cr\omega(\sin r + \sinh r)}. \tag{40}$$

Thus, we have determined the storage and loss moduli independent of the choice to impose oscillatory stress or velocity (or strain) on the plates and, indeed, as the asymptotic equations are linear, independent of the amplitude of the shear stress or plate velocity.

Figure 2 superimposes the storage and loss moduli effect for normal and tangential anchoring. We note that there is no qualitative difference in the dynamic moduli between the steady shear distinction of flow-aligning ($\lambda_L > 1$) and tumbling ($\lambda_L < 1$) nematic polymer regimes.[1] This result extends the same conclusion for dynamic moduli of

monodomains (Choate and Forest 2006). Thus, we plot only a representative case in the flow-aligning parameter regime with $a = 0.9$ ($\lambda_L = 1.04$). We observe that the effect of $\theta = 0$ on the moduli is simple scaling law:

$$G(\omega;\theta) = \Theta(\theta) G\left(\frac{\omega}{\Theta(\theta)};0\right), \tag{41}$$

where G is either G' or G''.

For normal anchoring, Eqs. 39 and 40 predict similar behavior of G' and G'' with respect to ω for nematic polymers as those found in Burghardt (1991) and de Andrade Lima and Rey (2006) for heterogeneous liquid crystals with normal anchoring. We discuss this behavior now to highlight the significant differences between normal anchoring and tan-

---

[1] As also observed in (de Andrade Lima and Rey 2004b), when $\lambda_L = 1$, we find purely viscous behavior for tangential anchoring with $G'(\omega) = 0$ and $G''(\omega) = C\omega$.

gential anchoring conditions, which were not analyzed in Burghardt (1991) and de Andrade Lima and Rey (2006).

Except for a region of moderate frequencies, the loss modulus $G''(\omega)$ exhibits nearly linear scaling behavior at high and low frequencies with a low frequency offset:

$$G''(\omega) = \left(C + \frac{B^2}{A}\right)\omega, \quad \text{as } w \to 0,$$
$$G''(\omega) = C\omega, \qquad\qquad \text{as } w \to \infty.$$
(42)

The constant offset between the high and low frequency limits, $\frac{B_2}{A} = \frac{3(1 \mp \lambda_L)^2}{4(s_0+2)}$, is always positive. However, we get an immediate insight into the difference between tangential and normal anchoring and rods versus platelets: for rods (when $\lambda_L \approx 1$) with normal anchoring, $B^2 = \frac{(1+\lambda_L)^2}{4} \approx 1$, whereas for tangential anchoring, $B^2 = \frac{(1-\lambda_L)^2}{4} \approx 0$. Thus, normal anchoring exhibits an increased loss modulus for low frequencies over tangential anchoring, but for high frequencies, the two anchoring conditions yield approximately the same values. However, for platelets, $\lambda_L \approx -1$ so that the effect of anchoring is reversed with tangential anchoring showing a low frequency increase over normal anchoring.

For the storage modulus, we also find different asymptotic regimes for high and low frequencies, but they have distinct scaling behaviors:

$$G'(\omega) = \frac{B^2}{12A^2}\omega^2, \qquad\qquad \text{as } w \to 0,$$
$$G'(\omega) = B^2 \sqrt{\frac{2C}{AC+B^2}}\sqrt{\omega}, \quad \text{as } w \to \infty$$
(43)

For reasons similar to the loss modulus behavior at low frequencies, the overall factor of B^2 is the dominant feature

Fig. 2 The effect of normal (solid lines) and tangential (dashed lines) anchoring on the dynamic moduli in the isotropic elasticity limit, $\theta=0$

in both regimes, accounting for the two to three orders of magnitude difference in $G'(\omega)$ between normal and tangential anchoring, shown in Fig. 2.

Now, we turn our attention to how these moduli predictions of heterogeneous polymers differ from a monodomain in shear flow (see Appendix and Choate and Forest 2006). Under the monodomain restriction, the stress tensor has only the viscous stress τ^{Vis} and the nematic elastic stress τ^{NE}, so that the shear stress 24 for monodomains reduces to

$$\tau^{(1)}_{xy,\,\text{monodomain}} = \left(\frac{\mu_1(s_0+2)}{6} + \frac{\mu_2 s_0^2}{4}\sin^2 2\psi_0 + \frac{\mu_3}{2}\right)\cos\omega t - \sin 2\psi_0 \frac{a\alpha}{2s_0^2}$$
$$\times \left((6 - N(2+s_0))s^{(1)} - (3 - N(2s_0+1))\beta^{(1)}\right).$$
(44)

In a sense, in terms of the elastic stress, monodomains represent the problem orthogonal to the present discussion of normal and tangential anchoring, which have only distortional elastic stresses. As observed in Larson and Mead (1989) and Choate and Forest (2006), a monodomain under the restriction to normal or tangential anchoring generates no elastic stresses so that $\mathbf{G'}(\omega)=0$ and $\mathbf{G''}(\omega)=C\omega$. However, with tilted anchoring, monodomains can give insight on the nematic elastic stress, in which case $s^{(1)}$ and $\beta^{(1)}$ are nonzero and the deviations of the order parameters from their equilibrium values become significant at leading order.

The major qualitative difference between the nematic elastic stress from a tilted monodomain from Appendix and
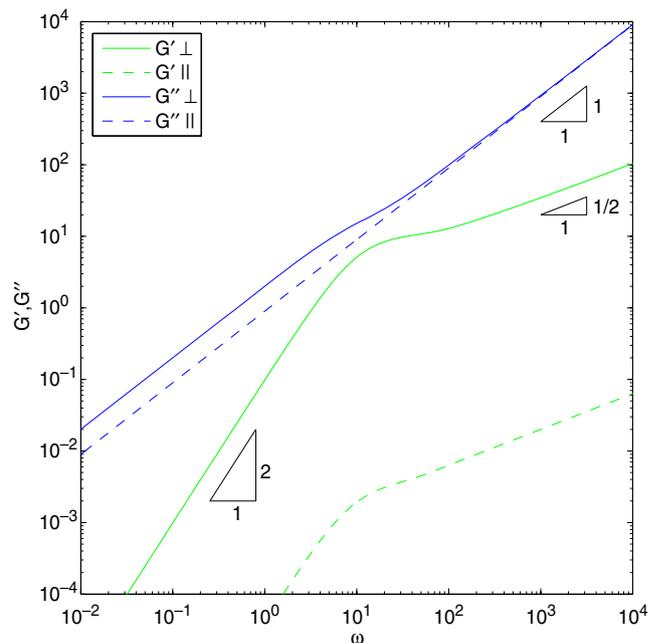
the distortional elastic stress from a heterogeneous sample with normal or tangential anchoring lies in the scaling law for $\mathbf{G'}(\omega)$ for high frequencies. For low frequencies, both models predict $O(\omega^2)$ scaling, but for monodomains, $G'(\omega)=O(1)$ as $w \to \infty$ in contrast to the scaling $G'(\omega) = O(\sqrt{\omega})$ found in Eq. 43.

Equivalence of flows

Now, we examine in further detail the equivalence of imposed velocity (or strain) and imposed stress boundary conditions inferred from the dynamic moduli. In the
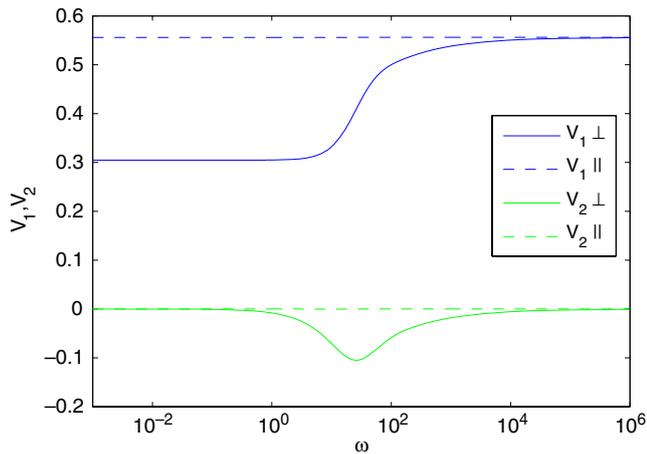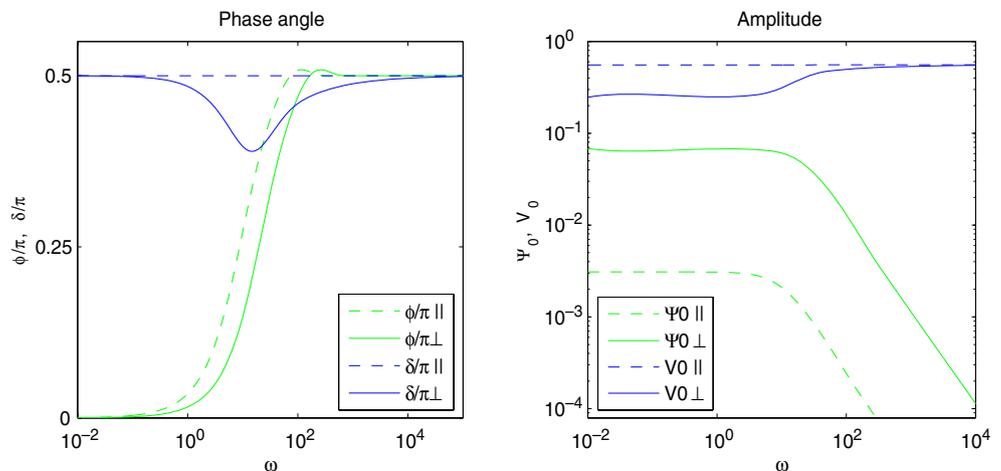
Fig. 3 The in-phase V_1 and out-of-phase V_2 responses of the upper plate velocity to imposed stress for tangential (*dashed lines*) and normal (*solid lines*) anchoring

following, the subscript τ indicates coefficients for imposed stress boundary conditions and the subscript υ for imposed velocity. The velocity-imposed boundary conditions easily translate to imposed strain as experimentally enforced by Noirez and collaborators (Pujolle-Robic and Noirez 2001; Mendil et al. 2005, 2006).

If a plate stress is imposed, then we have $\tau_{1,\tau}=1$ and $\tau_{2,\tau}=0$, and so from Eqs. 38 and 37,

$$V_{1,\tau} = E_2 \qquad\qquad V_{2,\tau} = -E_1,$$
$$C_{1,\tau} = \frac{2B}{C\omega}\frac{\sin\frac{r}{2}\sinh\frac{r}{2}}{\cosh r + \cos r}, \quad C_{2,\tau} = -\frac{2B}{C\omega}\frac{\cos\frac{r}{2}\cosh\frac{r}{2}}{\cosh r + \cos r}.$$

(45)

However, for imposed plate velocity, the boundary conditions are $V_{1,\upsilon}=1$ and $V_{2,\upsilon}=0$, and so

$$\tau_{1,\upsilon} = \frac{2G''}{\omega} = \frac{E_2}{E_1^2+E_2^2}, \tau_{2,\upsilon} = \frac{2G'}{\omega} = \frac{E_1}{E_1^2+E_2^2},$$
$$C_{1,\upsilon} = C_{1,\tau}\tau_{1,\upsilon} - C_{2,\tau}\tau_{2,\upsilon}, C_{2,\upsilon} = C_{2,\tau}\tau_{1,\upsilon} + C_{1,\tau}\tau_{2,\upsilon}.$$

(46)

It can be shown that within the gap, the solutions from these two boundary conditions differ only by a rescaling and a phase shift of $\chi = -\tan^{-1}\frac{E_1}{E_2}$:

$$\psi_\tau^{(1)}(y,t) = \sqrt{E_1^2 + E_2^2}\,\psi_\upsilon^{(1)}\left(y, t-\frac{\chi}{\omega}\right),$$
$$v_{x,\tau}^{(1)}(y,t) = \sqrt{E_1^2 + E_2^2}\,v_{x,\upsilon}^{(1)}\left(y, t-\frac{\chi}{\omega}\right).$$

(47)

For imposed stress, the velocity components of the upper plate are shown in Fig. 3. For tangential anchoring, there is no observable frequency dependence. For normal anchoring at high frequencies, the plate motion is the same as for tangential anchoring. However, for moderate frequencies, there is a significant out-of-phase response, and for lower frequencies, there is a significant decrease in the velocity compared to tangential anchoring, as indicated by the presence of the B^2 term, the low-frequency limit compared to the high-frequency limit:

$$\lim_{\omega\to 0} V_1 = \frac{A}{2(AC+B^2)}, \quad \lim_{\omega\to\infty} V_1 = \frac{1}{2C}.$$

(48)

To help us compare the macroscopic response of the velocity and the director angle with the imposed stress $\tau_{xy}^{(1)} = \cos\omega t$, we write the plate velocity as $V=V_0\cos$

Fig. 4 The phase angles with respect to the imposed stress δ (plate velocity) and ϕ (director angle at $y=0$), and the amplitudes V_0 (plates) and Ψ_0 (director angle at $y=0$)

($\omega t - \delta$), where $\tan \delta = \frac{G''}{G'}$ is the loss tangent, and we define $\Psi = \psi^{(1)}(0, t) = \Psi_0 \cos(\omega t - \phi)$ to be the director angle at the midpoint between the plates. Figure 4 shows plots of δ, ϕ, V_0, and Ψ_0 as functions of ω. The velocity is always out of phase with the stress by $\frac{\pi}{2}$ with the exception of a region of moderate frequencies for normal anchoring. The director angle is in phase with the stress for low frequencies, but for larger frequencies, it is in phase with the plates. This transition occurs at a lower frequency for tangential anchoring

than normal. The amplitude of the angle is constant for low frequencies, but is $O(\omega^{-1})$ for high frequencies and much larger for normal than tangential anchoring.

Pressure-driven Poiseuille flows

For small amplitude oscillatory pressure-driven flows, we proceed in a similar manner, seeking solutions to Eqs. 27–29 of the form 32. We find that

$$
\begin{aligned}
\psi_1(y) &= D_1 \ \cosh \ ry \ \sin \ ry + D_2 \ \sinh \ ry \ \cos \ ry, \\
\psi_2(y) &= -D_2 \ \cosh \ ry \ \sin \ ry + D_1 \ \sinh \ ry \ \cos \ ry - \frac{2B}{C\omega}y, \\
v_1(y) &= \frac{Br}{C}[(D_1 + D_2) \ \cosh \ ry \ \cos \ ry + (D_1 - D_2) \sinh \ ry \ \sin \ ry] + D_3 - \frac{y^2}{C}, \\
v_2(y) &= \frac{Br}{C}[(D_1 - D_2) \ \cosh \ ry \ \cos \ ry - (D_1 + D_2) \ \sinh \ ry \ \sin \ ry] + D_4
\end{aligned}
\tag{49}
$$

where r is the same as for oscillatory plate-driven shear. Applying the boundary conditions, $\psi_1(\pm 1) = \psi_2(\pm 1) = v_1(\pm 1) = v_2(\pm 1) = 0$ determines that

$$
\begin{aligned}
D_1 &= \frac{4B \cos r \sinh r}{C\omega(\cosh 2r - \cos 2r)}, \\
D_2 &= -\frac{4B \sin r \cosh r}{C\omega(\cosh 2r - \cos 2r)}, \\
D_3 &= \frac{1}{C} - \frac{2B^2 r(\sinh 2r - \sin 2r)}{C^2\omega(\cosh 2r - \cos 2r)}, \\
D_4 &= -\frac{2B^2 r(\sinh 2r + \sin 2r)}{C^2\omega(\cosh 2r - \cos 2r)}.
\end{aligned}
\tag{50}
$$

To define the storage and loss moduli, we must define a macroscopic shear rate. The natural choice is to measure the motion of the fluid at the middle of the gap relative to the bottom plate, and we define the velocity at the middle of the gap to be

$$
\begin{aligned}
V_1 &= v_1(0) = \frac{Br}{C}(D_1 + D_2) + D_3 = 2E_2, \\
V_2 &= v_2(0) = \frac{Br}{C}(D_1 - D_2) + D_4 = 2E_1,
\end{aligned}
\tag{51}
$$

where E_1 and E_2 are the same quantities defined in Eq. 38 for plate-driven flow. Thus, the motion of the midline of the fluid relative to the bottom plate in Poiseuille flow is the same as the motion of the top plate with respect to the bottom plate in plate-driven flow with imposed stress.

The Poiseuille stress components are simply $\tau_1 = -2y$ and $\tau_2 = 0$, and if we use the average stress $\overline{\tau}_{xy'}^{(1)} =$

$\int_{-1}^0 \tau_1 \cos \omega t + \tau_2 \sin \omega t \ dy = \cos \omega t$ to compute the storage and loss moduli relative to the macroscopic strain rate $\gamma = \frac{1}{\omega}(V_1 \sin \omega t - V_2 \cos \omega t)$, we find that $G'(\omega)$ and $G''(\omega)$ give exactly the same formulas as those for oscillatory plate-driven shear given by Eqs. 40 and 39. Thus, in a macroscopic sense, the bottom half of the channel in Poiseuille flow is "rheologically equivalent" to the plate-driven shear flow, where the middle of the pressure-driven flow corresponds to an oscillatory "plate" of fluid moving against a fixed bottom plate.

Heterogeneity of plate- and pressure-driven shear flows

We have carefully scaled the Poiseuille flow experiment so that from a macroscopic perspective, the bottom half of the fluid can be seen as a fluid trapped between two plates separated by the same distance, moving at the same relative velocity, and having the same average stress across the gap as the shear flow experiment with imposed stress boundary conditions. Furthermore, as $\psi^{(1)}$ is an odd function of y in Poiseuille flow, we effectively have the same anchoring conditions at the virtual top plate as the physical plate in the drag-driven flow. We now look closer to examine details of the interior gap responses, finding both similarities and differences in the detailed heterogeneity of the two flows.

First, the plate frequency induces a new length scale $\frac{1}{r}$, which defines a "boundary layer" near the plates with thickness proportional to $\frac{1}{\sqrt{\omega}}$. However, as the thickness of the boundary layer increases as the frequency decreases, if $\omega < 8\left(A + \frac{B^2}{C}\right)$, then in plate-driven flow the boundary

layers are thick enough that they overlap, filling the entire gap. This does not extend to the Poiseuille flow, as the boundary layer is present at the physical plate but not at the virtual plate!

In Fig. 5, we plot the velocity profiles of the two flows for normal anchoring. To plot them on the same coordinate axes, we have shifted the plate-driven flow so that the lower plate coincides with that of Poiseuille flow. Although the Poiseuille flow is slightly faster in both the in-phase and out-of-phase components, the out-of-phase components of both flows are only significant for moderate frequencies. For tangential anchoring, the velocity profiles have no significant dependence on ω.

In Fig. 6, we plot $\psi_i^*(y) = \frac{\psi_i(y)}{\Psi_0}$, which are the director angle profiles for both stress-driven and pressure-driven flows scaled by Ψ_0 from Fig. 4, the magnitude of $\psi^{(1)}$ halfway between the plates for plate-driven flow. Both flows have a similar dependence on the frequency in which, for low frequencies, ψ_1 is dominant with ψ_2 being insignificant. However, as ω increases, ψ_2 increases and, eventually, surpasses ψ_1 in dominance, although ψ_2 is $O(\omega^{-1})$ as $\omega \to \infty$. For low frequencies, the profiles of the two flows are quite similar in shape, but as the frequency increases, the profiles become quite dissimilar.

Parameter estimation from dynamic moduli measurements

We now turn our attention to the classical inverse problem of estimating material parameters of the nematic fluid from experimental measurements of the dynamic moduli. The following discussion is for rod-shaped macromolecules, but the strategies may be easily modified for disks. The predictions appear to be more practical for homeotropic anchoring because of a stronger signal-to-noise ratio. From Fig. 2 and from the scaling laws 42 and 43, we see two

distinct asymptotic regimes, one for high frequencies and another for low frequencies. We proceed by selecting representative frequencies from each regime, ω_{high} and ω_{low}, respectively, from which we use the values of the moduli for these frequencies to estimate parameters.

A classical problem for liquid crystals and liquid crystalline polymers is the determination of whether the nematic liquid is "flow aligning" or "tumbling" in steady shear from oscillatory shear experiments. Recall that for small molecule liquid crystals, the Leslie tumbling parameter is a material parameter, and the nematic liquid is characterized as either of two types (tumbling or flow-aligning in simple shear). For nematic polymers, however, the response in steady shear depends on the rigid-rod concentration (equivalently, strength of the excluded volume potential) and on the geometric aspect ratio of the rods. Several authors have made the distinction, including our group (Forest and Wang 2003). The general question remains: Can we determine the Leslie tumbling parameter λ_L defined earlier (Eq. 25) from oscillatory shear data?

From Eq. 42, we first note that, from the loss modulus in the high frequency limit, we can construct the ratio

$$C = \frac{G''_{\text{high}}}{\omega_{\text{high}}}. \tag{52}$$

Next, from the low frequency limit, the following relationship between the parameters is determined:

$$B^2 = A \frac{G''_{\text{low}} - C\omega_{\text{low}}}{\omega_{\text{low}}}. \tag{53}$$

We recall that $A = \frac{s_0+2}{3}$, and we observe that for normal anchoring conditions, $B = -\frac{1+\lambda_L}{2} < 0$. Thus,

$$B = -\sqrt{\frac{(s_0+2)\left(G''_{\text{low}} - C\omega_{\text{low}}\right)}{3\omega_{\text{low}}}}. \tag{54}$$

Fig. 5 The profiles of v_1 (*solid lines*) and v_2 (*dashed lines*) across the gap, for plate-driven flow with imposed stress and pressure-driven Poiseuille flow, both with normal anchoring
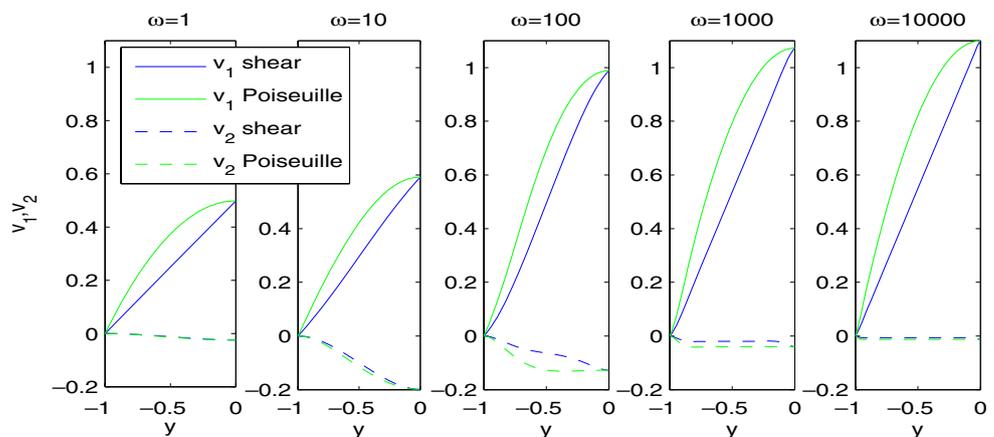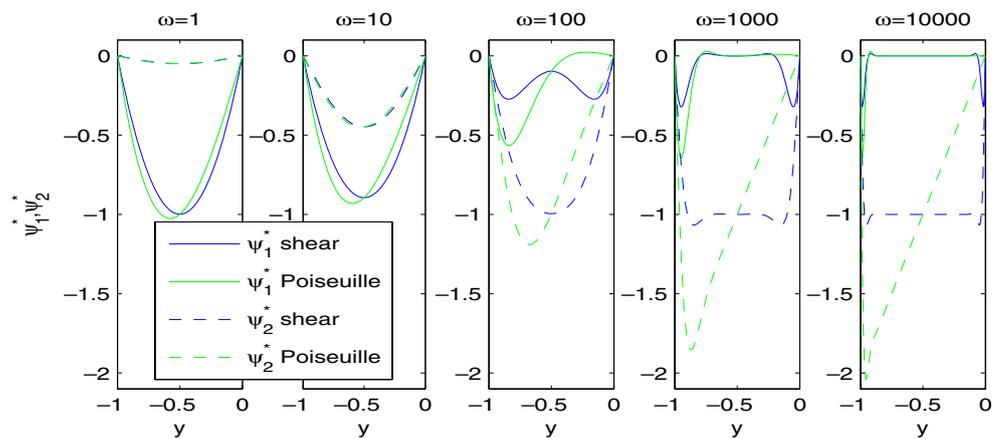
Fig. 6 The scaled in-phase ψ_1^* (*solid line*) and out-of-phase ψ_2^* (*dashed line*) director angles for normal anchoring

Therefore, we determine the Leslie parameter:

$$\lambda_{\rm L} = 2\sqrt{\frac{(s_0 + 2)\left(G_{\rm low}'' - C\omega_{\rm low}\right)}{3\omega_{\rm low}}} - 1. \tag{55}$$

Furthermore, for normal anchoring, we may assess the flow-aligning versus tumbling of a fluid by looking at B^2, which is greater than 1 for flow-aligning nematics and less than 1 for tumbling.

In a similar manner, we may infer a measure of the strength of the anisotropic distortional elasticity parameter θ through the following procedure. From the Θ scaling law for the moduli 41 and the low-frequency storage modulus scaling 43, we have that $G_{\rm low}'' = \frac{B^2\omega_{\rm low}^2}{12A^2\Theta}$, and so

$$\Theta(\theta) = \frac{B^2\omega_{\rm low}^2}{12A^2G_{\rm low}'} = \frac{\omega_{low}\left(G_{\rm low}'' - C\omega_{\rm low}\right)}{4(s_0 + 2)G_{\rm low}'}. \tag{56}$$

If normal anchoring conditions are used, the relative strength of the anisotropic distortional elasticity may be determined explicitly:

$$\theta = \frac{3}{1 + 2s_0}\left(\frac{\omega_{\rm low}\left(G_{\rm low}'' - C\omega_{\rm low}\right)}{4(s_0 + 2)G_{\rm low}'} - 1\right). \tag{57}$$

Conclusion

We have examined small amplitude oscillatory plate-driven and pressure-driven shear flows of nematic polymers, using a Doi–Hess–Marrucci–Greco mesoscopic tensor model. The analysis incorporates heterogeneity of the orientation and velocity fields and highlights the macroscopic effects of normal versus tangential anchoring at the plates on the bulk linear viscoelastic moduli. For these two special anchoring conditions, the nematic polymer response simplifies to an effective small-molecule liquid crystal response across the gap, and the flow-orientation tensor dynamics become explicitly solvable. We recover seminal results for plate-imposed stress and homeotropic anchoring of heterogeneous liquid crystals with one elasticity constant by Burghardt (1991) and de Andrade Lima and Rey (2006); we then extend their results to tangential anchoring. Furthermore, for these two special anchoring conditions, we determine the effects of anisotropic molecular elasticity (with two elasticity constants that have distinct ordering for rods and platelets) by virtue of a scaling symmetry of the governing equations.

Through a judicious nondimensionalization of the model equations, we show rheological equivalence between shear flows with imposed oscillatory stress, velocity (or strain), and pressure. That is, all experiments yield the same storage and loss moduli when anchoring conditions at the plates are identical (either tangential or homeotropic). An important physical prediction is the strong dependence of macroscopic storage and loss moduli on plate anchoring conditions, with two to three orders of magnitude enhancement of the storage modulus between normal and tangential anchoring. These predictions of a macroscopic influence of strong anchoring are consistent with the experimental results and interpretations of the Noirez group (Pujolle-Robic and Noirez 2001; Mendil et al. 2005, 2006). A deeper investigation into the effect of plate anchoring conditions is warranted, which will require numerical simulations, to determine whether the strongly elastic responses of liquid crystal polymers measured experimentally by Noirez et al. and Colby (Pujolle-Robic and Noirez 2001; Mendil et al. 2005, 2006; Colby et al. 2002) are captured by this model with tilted anchoring conditions both in and out of the shear plane and how the dynamic moduli and higher order harmonic response functions are modified in the nonlinear regime.

Appendix

The monodomain solution of Eqs. 20–24 is the restriction that $s^{(1)}$, $\beta^{(1)}$, and $\psi^{(1)}$ are constant with respect to y and that

$\frac{\partial v_x^{(1)}}{\partial y} = \cos \omega t$. Ignoring the long-time effects discussed in Choate and Forest (2006), this leads us to the storage and loss moduli

$$G'(\omega) = \sin^2 2\psi_0 \frac{a^2(1 - s_0)a_1 a_2}{6} \frac{\omega^2[a_2 + 3a_1(1 + 2s_0) + (a_1 + 3a_2(1 + 2s_0))\omega^2]}{\left(a_1^2 + \omega^2\right)\left(a_2^2 + \omega^2\right)}$$

$$G''(\omega) = \left(\frac{\mu_1(s_0 + 2)}{6} + \frac{\mu_2 s_0^2}{4}\sin^2 2\psi_0 + \frac{\mu_3}{2}\right)\omega \tag{58}$$

$$+ \sin^2 2\psi_0 \frac{a^2(1 - s_0)}{6} \frac{\omega[2a_1^2 a_2^2(2 + 3s_0) + (a_1^2 + 3a_2^2(1 + 2s_0))\omega^2]}{\left(a_1^2 + \omega^2\right)\left(a_2^2 + \omega^2\right)}$$

where $a_1 = 6\alpha N s_0$ and $a_2 = -2\alpha(6 - N(2 + s_0))$.

References

Burghardt WR (1991) Oscillatory shear flow of nematic liquid crystals. J Rheol 35:49–62

Choate EP, Forest MG (2006) A classical problem revisited: Rheology of nematic polymer monodomains in small amplitude oscillatory shear. Rheol Acta 46:83–94

Colby RH, Nentwich LM, Clingman SR, Ober CK (2002) Defect-mediated creep of structured materials. Europhys Lett 54:269–274

Cui Z, Forest MG, Wang Q, Zhou H (2006) On weak plane shear and Poiseuille flows of rigid rod and platelet ensembles. SIAM J Appl Math 66:1227–1260

de Andrade Lima LRP, Rey AD (2004a) Superposition and universality in the linear viscoelasticity of Leslie–Ericken liquid crystals. J Rheol 48:1067–1084

de Andrade Lima LRP, Rey AD (2004b) Assessing flow alignment of nematic liquid crystals through linear viscoelasticity. Phys Rev E 70:011701

de Andrade Lima LRP, Rey AD (2006) Superposition principles for small amplitude oscillatory shearing of nematic mesophases. Rheol Acta 45:591–600

Forest MG, Wang Q (2003) Monodomain response of finite-aspect-ratio macromolecules in shear and related linear flows. Rheol Acta 42:20–46

Forest MG, Wang Q, Zhou H (2000) Exact banded patterns from a Doi–Marrucci–Greco model of nematic liquid crystal polymers. Phys Rev E 61:6655–6662

Forest MG, Wang Q, Zhou H, Zhou R (2004) Structure scaling properties of confined nematic polymers in plane shear cells: the weak flow limit. J Rheol 48:175–192

Larson RG, Mead DW (1989) Linear viscoelasticity of nematic liquid crystalline polymers. J Rheol 33:185–206

Mather PT, Romo-Uribe A, Han CD, Kim SS (1997) Rheo-optical evidence of a flow-induced isotropic–nematic transition in a thermotropic liquid-crystalline polymer. Macromolecules 30:7977–7989

Mendil H, Baroni P, Noirez L (2005) Unexpected giant elasticity in side-chain liquid–crystal polymer melts: A new approach for the understanding of shear-induced phase transition. Europhys Lett 76:983–989

Mendil H, Baroni P, Noirez L (2006) Solid-like rheological response of non-entangled polymers in the molten state. Euro Phys J E 19:77–85

Pujolle-Robic C, Noirez L (2001) Observation of shear-induced nematic–isotropic transition in side-chain liquid crystal polymers. Nature 409:167–171

Rubin SF, Kannan RM, Kornfield JA, Boeffel C (1995) Effect of mesophase order and molecular weight on the dynamics of nematic and smectic side-group liquid-crystalline polymers. Macromolecules 28:3521–3530

Wang Q (2002) A hydrodynamic theory of nematic liquid crystalline polymers of different configurations. J Chem Phys 116:9120–9136

Zhou H, Forest MG (2006) Anchoring distortions coupled with plane Couette and Poiseuille flows of nematic polymers in viscous solvents: morphology in molecular orientation, stress, and flow. Discrete Contin Dyn Syst B 6:407–425

Zhou H, Forest MG (2007) Nematic liquids in weak capillary Poiseuille flow: Structure scaling laws and effective conductivity implications. International J Numer Anal Mod 4:460–477